Lateral Photovoltaic Effect in Silk-Protein-Based Nanocomposite Structure for Physically Transient Position-Sensitive Detectors

Yuhong Cao,[1,2] Zhuyikang Zhao,[1,2] Peng Bao,[1,2] Zhikai Gan,[3] and Hui Wang[1,2,*]

[1] *State Key Laboratory of Advanced Optical Communication Systems and Networks, School of Physics and Astronomy, Shanghai Jiao Tong University, 800 Dongchuan Road, Shanghai 200240, China*

[2] *Key Laboratory for Thin Film and Microfabrication Technology of the Ministry of Education, Research Institute of Micro/Nano Science and Technology, Shanghai Jiao Tong University, 800 Dongchuan Road, Shanghai 200240, China*

[3] *Key Laboratory of Infrared Imaging Materials and Detectors, Shanghai Institute of Technical Physics, Chinese Academy of Sciences, 500 Yutian Road, Shanghai 200083, China*

(Received 30 December 2020; revised 25 March 2021; accepted 16 April 2021; published 6 May 2021)

Silk protein is considered as an attractive transient biomaterial with fantastic properties applied to biophotoelectric devices. Combined with noble-metal silver nanoparticles, a transient composite structure of Ag nanoparticle-embedded silk protein (Ag/silk protein/Si) is constructed. We obtain a lateral photovoltaic effect with a maximum sensitivity of 308.3 mV/mm, which is a very large sensitivity value in the field of organic materials, even comparable to the reported sensitivities of most inorganic materials. We attribute this to the increase of photogenerated carriers at the illuminated spot caused by the local surface-plasmon resonance of silver particles and the effective regulation of the diffusion (or resistivity of the structure) of photogenerated carriers by a silk wrapper. Interestingly, both silk protein and silver have good biocompatibility, and the combination of the two might be an alternative for the future development of biomaterial-related transient photovoltaic devices.

DOI: 10.1103/PhysRevApplied.15.054011

I. INTRODUCTION

Transient electronic devices, an innovative evolution in modern electronics, refer to devices that can physically disappear on demand, have been widely investigated in a variety of applications [1–3], especially for an emerging field related to organic materials [4,5]. The natural biological material silk protein benefits from superior properties, such as being biocompatible, biodegradable, and environmentally friendly [6,7], which has paved the way toward many applications, including implantable bioelectronics, wearable technology, and green transient bioelectronic and photonic devices [6,8–10]. Additionally, silk protein possesses good film-forming properties, is low cost, and allows nanoscale processability. Therefore, transient electronic devices based on silk protein have gradually become an attractive research hotspot. In the past few years, Rogers *et al.* demonstrated that silk protein and other materials could be used to fabricate and integrate various transient electronic devices by combining a silicon-based complementary metal-oxide-semiconductor technique [1]. Wang *et al.* investigated the resistive switching effect based on silk protein as a substrate and switching layers for physically transient resistive switching memory [9]. Omenetto and co-workers put forward an inkjet-printing-based strategy to generate arbitrarily patterned photonic crystals based on silk inverse opal [11]. However, the characteristics of transient electronic devices, in particular, the lateral photovoltaic effect (LPE) based on silk protein, have barely been reported.

Here, we propose a simple transient nanocomposite structure of Ag/silk protein/Si fabricated on *n*-type silicon substrate. By adjusting the resistivity of Ag nanoparticles embedded in the silk-protein structure and combining the local surface-plasmon-resonance mechanism, we observe a very large lateral photovoltaic effect, with a sensitivity value of 308.3 mV/mm. It is well known, due to its output of lateral photovoltage (LPV) changing with light-spot position linearly, that LPE is mainly used in position-sensitive detectors (PSDs), which can detect very small displacement. It is reported that the best reported sensitivity value of most PSD devices based on organic materials, such as the structures of Al/poly(3-hexylthiophene-2,5-diyl) (P3HT) [12], poly(3,4-ethylenedioxythio-phene) polystyrene sulfonate (PEDOT:PSS):*n*-Si [13], ITO/PEDOT:PSS/poly (2-meth oxy-5 (2′-ethyl) hexoxy-phenylenevinylene) (MEH-PPV): phenyl-C61-butyric acid methyl ester (PCBM)/Al [14],

*huiwang@sjtu.edu.cn

roughly in the range of 2.97–106 mV/mm, the LPE sensitivity of our structure is much larger than these reported LPV
sensitivities based on organic materials. Our results are also comparable to the sensitivity of most inorganic (metal-oxide-) semiconductor structures, for example, GaAs/$Al_{0.3}Ga_{0.7}As$ [15], Ag/Sinanowires/*n*-Si [16], Ni/*p*-Si [17], and Ag-ZnO core-shell nanoparticles/*n*-Si [18], and some hot two-dimensional inorganic materials, such as $SnSe_2$/*p*-Si [19], Sb_2Se_3/*p*-Si [20], MoS_2/Si [21], and graphene/Ge [22]; the sensitivity values for these structures are roughly in the range of 50–499.24 mV/mm. Recently, Foisal *et al.* observed a giant value of LPV sensitivity (1780 mV/mm) in 3*C*-SiC/Si-Si-3*C*-SiC/Si structure [23]. However, this big sensitivity value is obtained as the distance between the two electrodes is only about 0.2 mm. Obtaining a large lateral photovoltaic effect in organic materials has been a challenge. Interestingly, silk fibroin, the most representative transient biomaterial, and the noble metal Ag, possessing unique optical properties and good biocompatibility [24,25], can both be processed in a water-based physiological environment; therefore, the combination of the two with light-sensitive silicon is expected to achieve a good transient LPV performance. Our results confirm this and we believe it may expand on opportunities for applications in biomedical devices based on silk fibroin.

II. EXPERIMENT

n-Type single-crystal Si (111) wafers (approximately 0.3-mm thick, 50–70 Ω cm resistivity) are used as substrates. Soluble lyophilized silk fibroin, purchased from Simatech Inc., is diluted in deionized (DI) water by ultrasonication for 15 min to form the silk fibroin solution (∼7 vol %), which is then filtered immediately using syringe filters of 0.45-μm aperture. Next, the silk fibroin solution is spin-coated on the Si substrates at 500 rpm for 5 s and 6000 rpm for 60 s and dried in air for 8 h.

The Ag (99.99%) nanoparticles are deposited on top of the silk protein/Si by dc magnetron sputtering at room temperature. The base pressure of the vacuum system prior to deposition is better than 2.2×10^{-4} Pa. During the process of deposition, an argon gas pressure of 0.72 Pa is maintained and the dc power is fixed at 20 W. The deposition rate of Ag is about 1.5Å s^{-1}, as determined by the stylus profile meter on thick calibration samples. In this work, four different Ag nominal thicknesses (discontinuous films) of 0.75, 1.05, 1.35, and 1.65 nm are prepared by adjusting the sputtering time.

LPV is measured by using a high-performance digital multimeter (34410A 6 1/2 Digit Multimeter, Agilent), and the position of the samples is controlled by a precise translation stage. The surfaces of samples are scanned spatially with a semiconductor laser (30 mW) focused into a roughly 50-μm-diameter spot, in background light to avoid spurious illumination. The topography information is acquired by a field-emission scanning electron microscope [18] (FESEM, Carl Zeiss Ultra 55, Germany, 5 kV). Surface-enhanced Raman scattering (SERS) is carried out with a handheld Raman spectrometer (BTC162-785S-OEM01, B&W Tek) under a 300-mW 785-nm semiconductor laser with an integration time of 1000 ms, and a Rhodamine 6G (R6G) aqueous solution (10^{-8} *M*) is used as a probe molecule. A finite-difference time domain (FDTD, Lumerical Solutions, Inc.) is applied to simulate the electric field distribution of the Ag/silk protein/Si structure, by setting periodic boundary conditions in both *x* and *y* directions, a perfectly matched layer in the *z* direction [26], and 635-nm plane wave along the *k*-direction propagation.

III. RESULTS AND DISCUSSION

The Ag/silk protein/Si three-layer structure model is shown in Fig. 1(a), where the layer of Ag defined as being of nominal thickness is composed of nanoparticles embedded in silk protein. For ease of visualization, Fig. 1(b) shows a simple diagram of Ag-embedded silk-protein nanostructure. The manufacturing process of samples is illustrated in Fig. 1(c). First, soluble lyophilized silk fibroin is dissolved in DI water. Then, the aqueous solution is spin-coated on cleaned silicon substrates. After crystallizing in air over 8 h, a uniform silk-fibroin film is formed. Lastly, Ag nanoparticles are deposited on the silk-fibroin layer using dc sputtering. Figure 1(d) is the cross-section SEM image of the silk protein/Si structure, and it shows that the thickness of silk protein is approximately 23 nm.

Figure 2 shows the morphological characteristics of samples determined by FESEM. Figure 2(a) is a very smooth surface of untreated silk protein film. Figures 2(c)

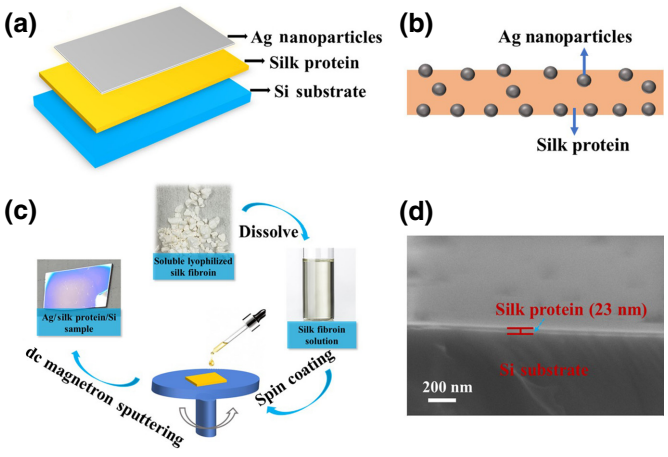

FIG. 1. (a) Structure of Ag/silk protein/Si sample. (b) Schematic illustration of Ag-embedded silk protein film. (c) Schematic diagram of Ag/silk protein/Si sample fabrication process. (d) Cross-section SEM image of silk protein/Si.

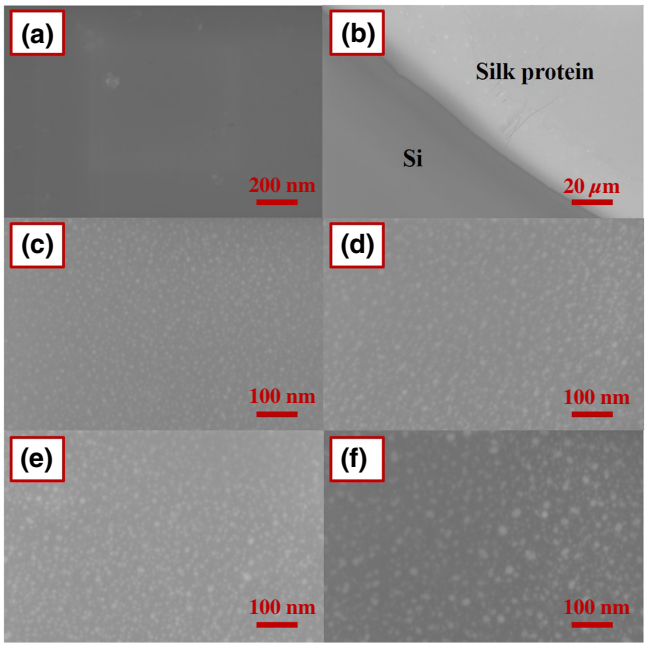

FIG. 2. SEM images (top view) of samples: (a) silk-fibroin layer, (b) boundary of silk fibroin and *n*-Si. (c)–(f) Deposited Ag nanoparticles on the surface of silk fibroin for four different nominal thicknesses, 0.75, 1.05, 1.35, and 1.65 nm, respectively.

to 2(f) exhibit the morphology distributions of Ag nanoparticles on silk-protein surfaces, with increasing sputtering time, corresponding to nominal thicknesses of 0.75, 1.05, 1.35, and 1.65 nm, respectively. Obviously, they are discontinuous films, and with an increase in the sputtering time, Ag nanoparticles with much larger sizes emerge, which is attributed to the increase in overall density and the formation of agglomerated Ag nanoparticles.

For the measurement of the LPV, the contacts (less than 1 mm in diameter) of all samples are formed by pressing copper wires with alloying indium and avoiding measurable rectifying behavior. The distance between two contacts (electrodes), A and B, is set as 1 mm, based on the distance effect of the contact points [27]. The schematics are shown in the insets of Figs. 3(a) and 3(b).

Initially, we discuss the results for the LPE of different structures (Si, silk/Si and Ag/silk protein/Si) with a 635-nm laser (30 mW), as shown in Fig. 3(a). In Ag/silk protein/Si structures, the Ag nominal thicknesses varies from 0.75 to 1.65 nm. Notably, the LPV output always changes nearly linearly with the laser position being moved between A and B, which behaves similarly to previous works [16,28–30]. The LPV reaches its maximum value when the laser spot moves to the two electrodes, and the value gradually linearly decreases to zero, when the laser spot moves from the electrodes to the midpoint.

Moreover, the variation of LPV to a unit displacement of the laser spot is defined as sensitivity [27], which is an important criterion for characterizing the LPE. The sensitivity variation of different Ag nominal thicknesses is illustrated in Fig. 3(c), corresponding to Fig. 3(a). Apparently, the structure with an Ag nominal thickness of 1.05 nm has the strongest LPE, and its sensitivity reaches up to 308.3 mV/mm, which is comparable to most inorganic materials, even beyond. When the Ag thickness deviates from the optimal thickness, the sensitivity value drops sharply. As a control, the LPV signal on the bare *n*-Si surface is very weak, and its sensitivity is only 4.7 mV/mm [blue one in Fig. 3(a)]. The silk protein/Si sample can result in a slight increase of the LPV sensitivity to 6.6 mV/mm [dark yellow one in Fig. 3(a)]. However, they the values for these samples are still much smaller than those of Ag/silk protein/Si samples, including the sensitivity observed in Ag/*n*-Si structures (maximum 1.24 mV/mm) we prepared earlier [16].

To gain a further insight into the relationship between the LPV and the laser wavelengths, we test the LPV at different wavelengths in the sample with the strongest LPE [Ag (1.05 nm)/silk protein/Si]. As shown in Fig. 3(b), the sample is irradiated by different laser wavelengths at a fixed power of 30 mW (532, 635, 780, and 980 nm, i.e., in the dark), and the sensitivity values are shown in Fig. 3(d). Very similar to our previous reports [31], there is also an optimal wavelength in these experiments; the strongest effect appears at 635 nm. Our results show the Ag/silk protein/Si structures can be an outstanding candidate in both visible-region and near-infrared biodetections.

The physical mechanism behind this LPV can be described as follows. During the sputtering process, some Ag nanoparticles easily penetrate the thin silk layer and deposit on the Si surface, forming metal-semiconductor Schottky barriers. When the laser illuminates the surface of the metal-semiconductor structure (Ag and Si in this work), the equilibrium state of the Schottky barrier will be broken, giving rise to the generation of photogenerated carriers locally at the illuminated spot of Si. Then, the photogenerated electron-hole pairs (EHPs) will be separated by the built-in electric field. The photogenerated holes diffuse along the interface, forming a certain concentration gradient in the lateral direction, while photogenerated electrons diffuse in the silicon side. Once the carrier concentration at any two points on the same side is different, then the output of the LPV will be detected.

As shown in Figs. 3(a) and 3(b), the LPV approximately varies linearly with x, and this is consistent with the theoretical model [27,32,33]:

$$V_{\mathrm{lat}}(x) = \frac{2KN}{\lambda} \exp\left(-\frac{L/2}{\lambda}\right) x, \tag{1}$$

where N is the photogenerated carrier density at light point x; K is the proportional coefficient related to the Fermi level. λ is the electron-diffusion length in the metal

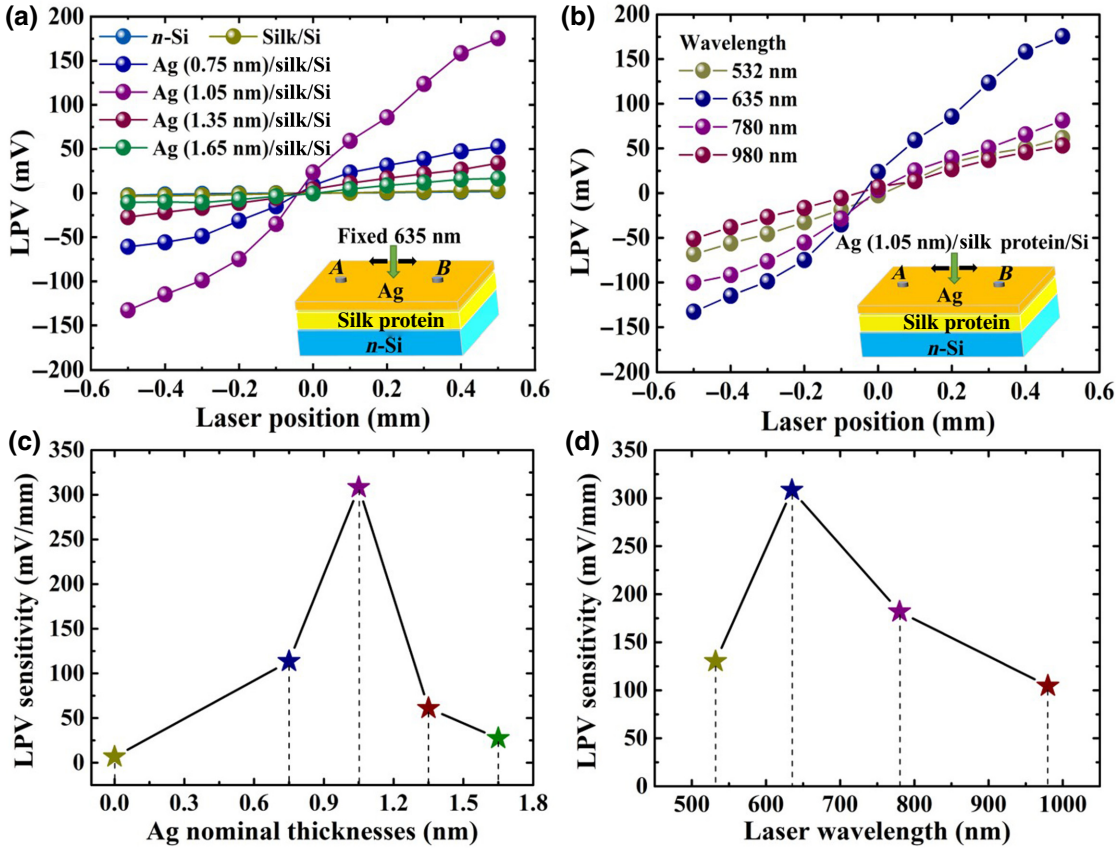

FIG. 3. (a) LPVs of Ag/silk protein/Si structures with different Ag nominal thicknesses. Inset in the bottom right is schematic diagram for LPV measurements (*A*-*B* distance, 1 mm; middle point is set as zero position). Incident laser is 635 nm with power fixed at 30 mW. (b) LPV of Ag (1.05 nm)/silk protein/Si under laser irradiation of different wavelengths with power fixed at 30 mW. (c) Sensitivity of different Ag nominal thicknesses, corresponding to (a). (d) Sensitivity of Ag (1.05 nm)/silk protein/Si sample under different wavelengths, corresponding to (b).

film, depending on the thickness of the Ag film. L is the distance between the two contacts. Furthermore, the sensitivity, defined as a variation of LPV to a unit displacement of the laser spot, can be defined as

$$\text{sensitivity} = \frac{d(V_{\text{lat}})}{dx} = \frac{2KN}{\lambda}\exp\left(-\frac{L/2}{\lambda}\right). \quad (2)$$

We believe the Ag-embedded silk protein can greatly enhance the LPE of the structure due to two dominant factors, namely, the diffusion length (or resistivity) and the carrier concentration at the laser irradiation position.

First, according to Eq. (2), the LPV sensitivity is connected to diffusion length λ and $\lambda \propto \rho^{-1/2}$ [27], that is, the sensitivity is related to the resistivity of the sample. It is not difficult to understand that, if the resistivity is very small, λ is almost infinite, which means that electrons easily diffuse from the light point to the sides, leading to no potential difference and an equipotential surface. On the contrary, if the resistivity is huge, it is difficult for electrons to diffuse from the light point to both sides due to the very small λ, which also results in a small potential-energy difference between the two contact points. Therefore, an optimal resistivity must exist between the two situations. It is easy to understand that the proper mixing of silk fibroin and silver can effectively adjust the resistivity of the structure. This is why we can experimentally observe a large LPV with an optimal thickness in Ag/silk protein/Si structures [please see Fig. 3(a)]. This result is consistent with our previous results reported in other structures [16–18,27,30,31].

Second, in general, noble metals [e.g., gold (Au) and silver (Ag)], can trigger localized surface-plasmon resonances (LSPR) [34] under incident-light irradiation, mainly based on the electromagnetic enhancement of active surfaces [35]. Then, through abundant localized plasmon excitations ("hot spots"), the SERS performance will be probed. In Ag/silk protein/Si nanostructures, the presence of Ag metal particles is also very likely to trigger LSPR. However, because of the biocompatible and degradable nature oof silk protein, Ag-embedded silk-fibroin film will be dissolved and separate rapidly in an

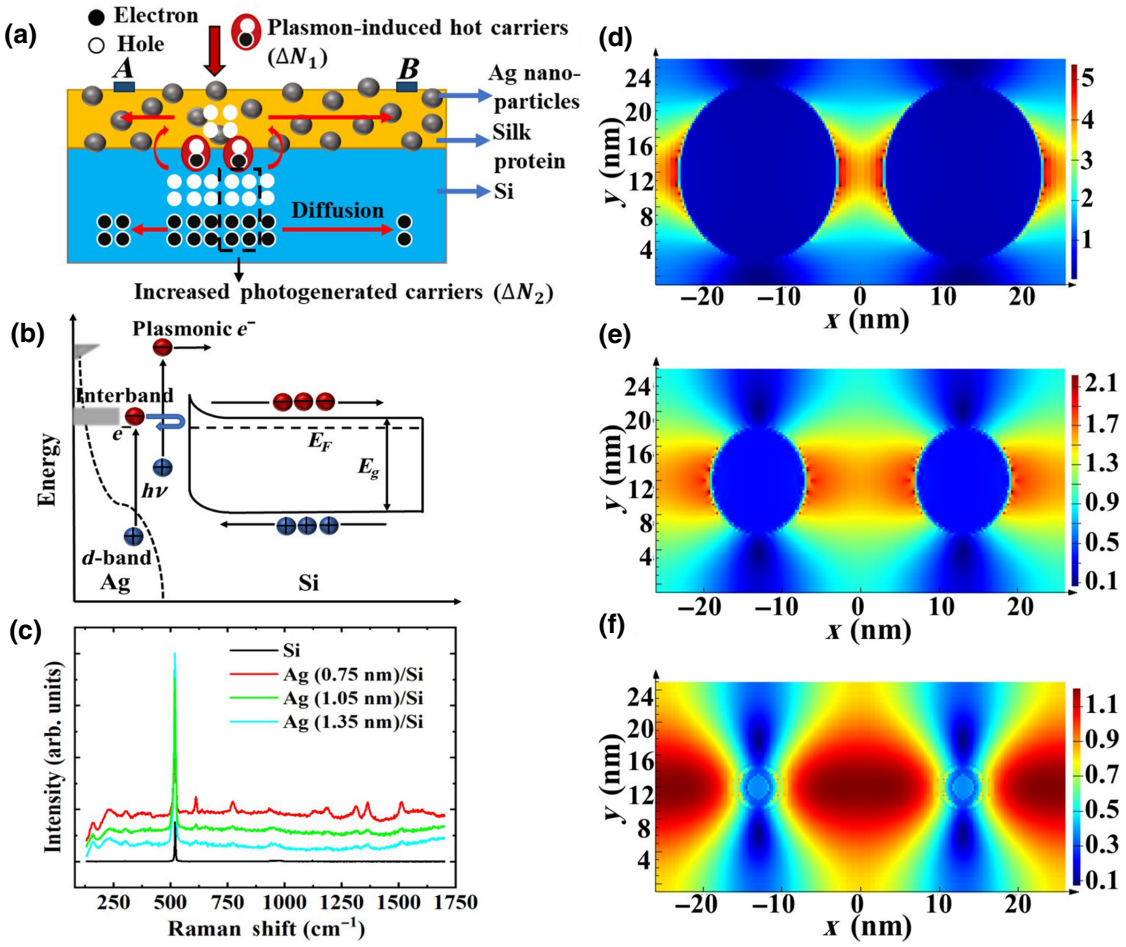

FIG. 4. (a) Schematic of enhanced LPE in Ag/silk protein/Si based on LSPR. (b) Energy-band diagram at interface of Ag nanoparticles and Si. (c) SERS spectra of 10^{-8} M R6G obtained on different structures, including bare n-Si substrate, Ag (0.75 nm)/Si, Ag (1.05 nm)/Si, and Ag (1.35 nm)/Si. (d)–(f) FDTD-simulated electric field intensity of Ag/silk protein/Si structure, corresponding to x-y plane at $z = 0$, $z = 8$, and $z = 10$ nm, respectively.

aqueous environment. To check the existence of LSPR, we use Ag/Si instead of Ag/silk protein/Si. As shown in Fig. 4(c), for bare Si without Ag nanoparticles, the Raman signal does not appear. Once Ag nanoparticles are deposited onto Si surfaces, the Raman signals can be obviously detected with characteristic peaks [16] at 611, 768, 1181, 1309, 1360, 1508, and 1648 cm^{-1}. Moreover, as shown in Fig. 4(c), we find that the intensity of the Raman signal is related to the thickness of the deposited Ag metal particles (nominal thickness), mainly due to the size effect of nanoparticles on SERS [36].

To further confirm the existence of LSPR in the response process of the LPE, the FDTD method is employed to numerically simulate the electromagnetic response for the Ag nanocomposite structure. In view of SEM characterization (Fig. 2), the average diameter of Ag nanoparticles is calculated to be 20 nm for the Ag(1.05 nm)/silk protein/Si structure. Hence, a model with 20-nm-diameter Ag nanospheres and a gap of 26 nm between two neighboring Ag nanoparticles is set. Additionally, a refractive index model is built to simulate the silk-protein film, which is measured to have an index of refraction of 1.54 (at 633 nm) [37]. The spatial distributions of the simulated electric field intensity (color bar) are illustrated in Figs. 4(d)–4(f), corresponding to the x-y plane at $z = 0$, $z = 8$, $z = 10$ nm, respectively. From FDTD simulation results, between two Ag nanoparticles, there is a remarkable localized resonant-field enhancement and the strongest signal appears close to the Ag nanoparticle surface. This indicates that the Ag/silk protein/Si structure possesses a strong LSPR.

According to the Raman experiment and FDTD simulation results, in Ag/silk protein/Si structures, the approaches to boost the generation of carriers coming from a strong LSPR around Ag nanoparticles are mainly triggered by two processes [please refer to Fig. 4(a)]. One is the plasmon-induced hot carriers, ΔN_1 (intraband carriers), which have a higher energy to overcome the barrier from the Ag

interface to Si than that of interband carriers [38], as shown in Fig. 4(b). ΔN_1 is proportional to the integrating optical absorption power, P_{MFP}. P_{MFP} can be related to the incident-light-source frequency, ω; local electric field strength, $|\mathbf{E}|^2$; and the imaginary part of the dielectric permittivity, $\mathrm{Im}(\varepsilon)$, then integrating over an effective volume, V_{MFP}, within the mean-free path l_{MFP} [38]

$$P_{\mathrm{MFP}} = \frac{1}{2}\int_{V_{\mathrm{MFP}}} d\mathbf{r}\omega|\mathbf{E}(\mathbf{r})|^2\mathrm{Im}(\varepsilon), \tag{3}$$

$$\Delta N_1 \propto \int P_{\mathrm{MFP}} dV. \tag{4}$$

The other one is from the increase of photogenerated carriers caused by enhanced light absorption. It is well accepted that LSPR can increase light absorption near metal-semiconductor interfaces [39–41]. Obviously, this part of the increased light helps to generate more electron-hole pairs. We describe this part of the photogenerated carriers as ΔN_2. Therefore, the total extra photogenerated carriers (LSPR + absorption enhancement) ΔN is

$$\Delta N = \Delta N_1 + \Delta N_2 \propto \int P_{\mathrm{MFP}} dV + \Delta N_2. \tag{5}$$

Combined with Eq. (2), the photogenerated carrier density, N, at the light point is increased by $\Delta N_1 + \Delta N_2$, resulting in an increase in sensitivity.

IV. CONCLUSION

We clearly demonstrate the LSPR-dominated LPE with a large sensitivity of 308.3 mV/mm in Ag/silk protein/Si structures. We believe that this represents a definitive observation of the transient LPE based on silk protein, suggesting it as an attractive candidate for the scalable implementation of high-quality transient photovoltaic devices.

ACKNOWLEDGMENTS

This work is supported by the National Natural Science Foundation of China under Grants No. 11874041, No. 61574090, No. 11374214, No. 10974135, and No. 62004203. The authors would like to thank Ms. W. Jiang from Advanced Electronic Materials and Devices (AEMD) of Shanghai Jiao Tong University for their technical assistance.

[1] S.-W. Hwang, H. Tao, D.-H. Kim, H. Cheng, J.-K. Song, E. Rill, M. A. Brenckle, B. Panilaitis, S. M. Won, Y.-S. Kim, *et al.*, A physically transient form of silicon electronics, Science. **337**, 1640 (2012).

[2] L. Yin, H. Cheng, S. Mao, R. Haasch, Y. Liu, X. Xie, S.-W. Hwang, H. Jain, S.-K. Kang, Y. Su, *et al.*, Dissolvable metals for transient electronics, Adv. Funct. Mater. **24**, 645 (2014).

[3] S.-K. Kang, S.-W. Hwang, S. Yu, J.-H. Seo, E. A. Corbin, J. Shin, D. S. Wie, R. Bashir, Z. Ma, and J. A. Rogers, Biodegradable thin metal foils and spin-on glass materials for transient electronics, Adv. Funct. Mater. **25**, 1789 (2015).

[4] H. Jeong, S. Baek, S. Han, H. Jang, S. H. Kim, and H. S. Lee, Novel eco-friendly starch paper for use in flexible, transparent, and disposable organic electronics, Adv. Funct. Mater. **28**, 1704433 (2018).

[5] D. Ye, X. Lei, T. Li, Q. Cheng, C. Chang, L. Hu, and L. Zhang, Ultrahigh tough, super clear, and highly anisotropic nanofiber-structured regenerated cellulose films, ACS Nano. **13**, 4843 (2019).

[6] D.-H. Kim, J. Viventi, J. J. Amsden, J. Xiao, L. Vigeland, Y.-S. Kim, J. A. Blanco, B. Panilaitis, E. S. Frechette, D. Contreras, *et al.*, Dissolvable films of silk fibroin for ultrathin conformal bio-integrated electronics, Nat. Mater. **9**, 511 (2010).

[7] S. H. Kim, Y. K. Yeon, J. M. Lee, J. R. Chao, Y. J. Lee, Y. B. Seo, M. T. Sultan, O. J. Lee, J. S. Lee, S.-i. Yoon, *et al.*, Precisely printable and biocompatible silk fibroin bioink for digital light processing 3D printing, Nat. Commun. **9**, 1620 (2018).

[8] S.-W. Hwang, D.-H. Kim, H. Tao, T.-i. Kim, S. Kim, K. J. Yu, B. Panilaitis, J.-W. Jeong, J.-K. Song, F. G. Omenetto, *et al.*, Materials and fabrication processes for transient and bioresorbable high-performance electronics, Adv. Funct Mater. **23**, 4087 (2013).

[9] H. Wang, B. Zhu, X. Ma, Y. Hao, and X. Chen, Physically transient resistive switching memory based on silk protein, Small. **12**, 2715 (2016).

[10] S. Kim, A. N. Mitropoulos, J. D. Spitzberg, H. Tao, D. L. Kaplan, and F. G. Omenetto, Silk inverse opals, Nat. Photonics. **6**, 818 (2012).

[11] W. Li, Y. Wang, M. Li, L. P. Garbarini, and F. G. Omenetto, Inkjet printing of patterned, multispectral, and biocompatible photonic crystals, Adv. Mater. **31**, 1901036 (2019).

[12] D. Kabra, T. B. Singh, and K. S. Narayan, Semiconducting-polymer-based position-sensitive detectors, Appl. Phys. Lett. **85**, 5073 (2004).

[13] M. Javadi, M. Gholami, H. Torbatiyan, and Y. Abdi, Hybrid organic/inorganic position-sensitive detectors based on PEDOT: PSS/n-Si, Appl. Phys. Lett. **112**, 113302 (2018).

[14] M. Zhu, K. Meng, C. Xu, J. Zhang, and G. Ni, Lateral photovoltaic effect in ITO/PEDOT:PSS/MEH-PPV:PCBM/Al organic photovoltaic cells, Org. Electron. **78**, 105585 (2020).

[15] J. H. Liu, S. Qiao, B. Liang, S. Wang, and G. Fu, Lateral photovoltaic effect observed in doping-modulated $GaAs/Al_{0.3}Ga_{0.7}As$, Opt. Express. **25**, A166 (2017).

[16] C. Mei, S. Liu, X. Huang, Z. Gan, P. Zhou, and H. Wang, Localized surface plasmon induced position-sensitive photodetection in silicon-nanowire-modified Ag/Si, Small. **13**, 1701726 (2017).

[17] X. Huang, C. Mei, Z. Gan, P. Zhou, and H. Wang, Lateral photovoltaic effect in p-type silicon induced by surface states, Appl. Phys. Lett. **110**, 121103 (2017).

[18] X. Dong, D. Zheng, J. Lu, Y. Niu, B. Liu, and H. Wang, Plasmon-enhanced lateral photovoltaic effect observed in

Ag-ZnO core–shell nanoparticles, Appl. Phys. Lett. **118**, 122101 (2021).

[19] T. Xu, Y. Han, L. Lin, J. Xu, Q. Fu, H. He, B. Song, Q. Gai, and X. Wang, Self-power position-sensitive detector with fast optical relaxation time and large position sensitivity basing on the lateral photovoltaic effect in tin diselenide films, J. Alloys Compd. **790**, 941 (2019).

[20] Y. Zhang, Y. Zhang, T. Yao, C. Hu, Y. Sui, and X. Wang, Ultrahigh position sensitivity and fast optical relaxation time of lateral photovoltaic effect in Sb_2Se_3/p-Si junctions, Opt. Express. **26**, 34214 (2018).

[21] R. Cong, S. Qiao, J. Liu, J. Mi, W. Yu, B. Liang, G. Fu, C. Pan, and S. Wang, Ultrahigh, ultrafast, and self-powered visible-near-infrared optical position-sensitive detector based on a CVD-prepared vertically standing few-layer MoS_2/Si heterojunction, Adv. Sci. **5**, 1700502 (2018).

[22] K. Liu, W. Wang, Y. Yu, X. Hou, Y. Liu, W. Chen, X. Wang, J. Lu, and Z. Ni, Graphene-based infrared position-sensitive detector for precise measurements and high-speed trajectory tracking, Nano Lett. **19**, 8132 (2019).

[23] A. R. M. Foisal, A. Qamar, T. Nguyen, T. Dinh, H. P. Phan, H. Nguyen, P. G. Duran, E. W. Streed, and D. V. Dao, Ultrasensitive self-powered position-sensitive detector based on horizontally-aligned double 3C-SiC/Si heterostructures, Nano Energy. **79**, 105494 (2021).

[24] S. Choi, S. I. Han, D. Jung, H. J. Hwang, C. Lim, S. Bae, O. K. Park, C. M. Tschabrunn, M. Lee, S. Y. Bae, *et al.*, Highly conductive, stretchable and biocompatible Ag − Au core–sheath nanowire composite for wearable and implantable bioelectronics, Nat. Nanotechnol. **13**, 1048 (2018).

[25] Z. Wang, S. Joshi, S. Savel'ev, W. Song, R. Midya, Y. Li, M. Rao, P. Yan, S. Asapu, Y. Zhuo, *et al.*, Fully memristive neural networks for pattern classification with unsupervised learning, Nat. Electron. **1**, 137 (2018).

[26] P. Biagioni, J. S. Huang, L. Duò, M. Finazzi, and B. Hecht, Cross Resonant Optical Antenna, Phys. Rev. Lett. **102**, 256801 (2009).

[27] C. Q. Yu, H. Wang, S. Q. Xiao, and Y. X. Xia, Direct observation of lateral photovoltaic effect in nano-metal-films, Opt. Express. **17**, 21712 (2009).

[28] C. Q. Yu and H. Wang, Light-induced bipolar-resistance effect based on metal–oxide–semiconductor structures of Ti/SiO_2/Si, Adv. Mater **22**, 966 (2010).

[29] B. Zhang, L. Du, and H. Wang, Bias-assisted improved lateral photovoltaic effect observed in Cu_2O nano-films, Opt. Express. **22**, 1661 (2014).

[30] Z. Gan, P. Zhou, X. Huang, C. Mei, K. Zhang, and H. Wang, Using electric pulse and laser to trigger a sharp and non-volatile change of lateral photovoltage in nano-carbon film, Appl. Phys. Lett. **108**, 131111 (2016).

[31] C. Q. Yu and H. Wang, Large near-infrared lateral photovoltaic effect observed in Co/Si metal-semiconductor structures, Appl. Phys. Lett. **96**, 171102 (2010).

[32] S. Liu, H. Wang, Y. Yao, L. Chen, and Z. Wang, Lateral photovoltaic effect observed in nano Au film covered two-dimensional colloidal crystals, Appl. Phys. Lett. **104**, 111110 (2014).

[33] A. Dong and H. Wang, Lateral photovoltaic effect and photo-induced resistance effect in nanoscale metal-semiconductor systems, Ann. Phys-Berlin. **531**, 1800440 (2019).

[34] H. Lee, J.-H. Lee, S. M. Jin, Y. D. Suh, and J.-M. Nam, Single-molecule and single-particle-based correlation studies between localized surface plasmons of dimeric nanostructures with ∼1 nm gap and surface-enhanced raman scattering, Nano. Lett. **13**, 6113 (2013).

[35] S. Nie and S. R. Emory, Probing single molecules and single nanoparticles by surface-enhanced raman scattering, Science. **275**, 1102 (1997).

[36] A. Gellé, T. Jin, L. de la Garza, G. D. Price, L. V. Besteiro, and A. Moores, Applications of plasmon-enhanced nanocatalysis to organic transformations, Chem. Rev. **120**, 986 (2020).

[37] S. T. Parker, P. Domachuk, J. Amsden, J. Bressner, J. A. Lewis, D. L. Kaplan, and F. G. Omenetto, Biocompatible silk printed optical waveguides, Adv. Mater. **21**, 2411 (2009).

[38] B. Y. Zheng, H. Zhao, A. Manjavacas, M. McClain, P. Nordlander, and N. J. Halas, Distinguishing between plasmon-induced and photoexcited carriers in a device geometry, Nat. Commun. **6**, 7797 (2015).

[39] M. L. Brongersma, N. J. Halas, and P. Nordlander, Plasmon-induced hot carrier science and technology, Nat. Nanotechnol. **10**, 25 (2015).

[40] M. W. Knight, H. Sobhani, P. Nordlander, and N. J. Halas, Photodetection with active optical antennas, Science. **332**, 702 (2011).

[41] H. A. Atwater and A. Polman, Plasmonics for improved photovoltaic devices, Nat. Mater. **9**, 205 (2010).